

## Inhibition, Escape, and Attenuated Growth of Severe Acute Respiratory Syndrome Coronavirus Treated with Antisense Morpholino Oligomers†

Benjamin W. Neuman,<sup>1\*</sup> David A. Stein,<sup>4</sup> Andrew D. Kroeker,<sup>4</sup> Michael J. Churchill,<sup>2</sup>  
Alice M. Kim,<sup>1</sup> Peter Kuhn,<sup>2</sup> Philip Dawson,<sup>2,3</sup> Hong M. Moulton,<sup>4</sup>  
Richard K. Bestwick,<sup>4</sup> Patrick L. Iversen,<sup>4</sup>  
and Michael J. Buchmeier<sup>1</sup>

*The Scripps Research Institute, Division of Virology, Department of Neuropharmacology,<sup>1</sup> and Department of Cell Biology,<sup>2</sup> and Skaggs Institute for Chemical Biology,<sup>3</sup> 10550 North Torrey Pines Rd., La Jolla, California 92037, and AVI BioPharma Inc., 4575 SW Research Way, Corvallis, Oregon 97333<sup>4</sup>*

Received 10 November 2004/Accepted 4 April 2005

The recently emerged severe acute respiratory syndrome coronavirus (SARS-CoV) is a potent pathogen of humans and is capable of rapid global spread. Peptide-conjugated antisense morpholino oligomers (P-PMO) were designed to bind by base pairing to specific sequences in the SARS-CoV (Tor2 strain) genome. The P-PMO were tested for their capacity to inhibit production of infectious virus as well as to probe the function of conserved viral RNA motifs and secondary structures. Several virus-targeted P-PMO and a random-sequence control P-PMO showed low inhibitory activity against SARS coronavirus. Certain other virus-targeted P-PMO reduced virus-induced cytopathology and cell-to-cell spread as a consequence of decreasing viral amplification. Active P-PMO were effective when administered at any time prior to peak viral synthesis and exerted sustained antiviral effects while present in culture medium. P-PMO showed low nonspecific inhibitory activity against translation of nontargeted RNA or growth of the arenavirus lymphocytic choriomeningitis virus. Two P-PMO targeting the viral transcription-regulatory sequence (TRS) region in the 5' untranslated region were the most effective inhibitors tested. After several viral passages in the presence of a TRS-targeted P-PMO, partially drug-resistant SARS-CoV mutants arose which contained three contiguous base point mutations at the binding site of a TRS-targeted P-PMO. Those partially resistant viruses grew more slowly and formed smaller plaques than wild-type SARS-CoV. These results suggest PMO compounds have powerful therapeutic and investigative potential toward coronavirus infection.

The perception of coronaviruses as harmless seasonal pathogens was indelibly changed in 2002, with the emergence of severe acute respiratory syndrome, a severe, sometimes fatal respiratory disease. Thanks in part to the availability of severe acute respiratory syndrome coronavirus (SARS-CoV) bioinformatics and structural data, identification of potential SARS-CoV antiviral compounds has moved rapidly. For example, antiviral compounds which target the SARS-CoV superfamily 1 helicase and the 3C-related serine proteinase with 50% effective concentration ( $EC_{50}$ ) values in the low micromolar range have been reported (1, 19, 20, 44). However, the second SARS-CoV-encoded proteinase, a papain-related cysteine proteinase, may prove to be a less suitable drug target, as a coronavirus molecular clone lacking one of the two known cleavage sites for this enzyme displayed only minor growth defects in cell culture (7).

Other confirmed and putative viral enzymes, including the polymerase, poly(U)-specific endoribonuclease homolog, S-adenosylmethionine-dependent ribose 2'-O-methyltransferase,

and cyclic phosphodiesterase, are potential anti-SARS drug targets (34). Furthermore, not all proposed SARS-CoV inhibitors act by inhibiting viral enzymes. Compounds targeting the interaction of the viral spike protein with the ACE-2 receptor (20, 44, 45) or with the spike-mediated fusion event (3, 14, 22, 47) and showing micromolar-scale efficiency in cell culture have been reported. Several groups have also reported in vitro efficacy with small interfering RNAs (42, 48) targeted at suppression of viral gene expression.

Compounds designed to function by base pairing to specific nucleic acid sequences, collectively known as antisense agents, offer a potentially powerful and selective tool for manipulating host and pathogen gene expression. Antisense agents directed against single-stranded RNA are known to act by two general mechanisms: by causing damage to an RNA strand containing the complementary "target" sequence through priming of endogenous RNase H activity, or by steric interference with targeted RNA function. Phosphorodiamidate morpholino oligomers (PMO) act by the latter mechanism, duplexing to specific RNA sequence by Watson-Crick base-pairing and forming a steric block (37).

The most frequently successful strategies for PMO-based gene knockdown are inhibiting translation initiation (28) and mRNA splicing (9). We recently demonstrated the antiviral effects of one peptide-conjugated PMO (P-PMO) complemen-

\* Corresponding author. Mailing address: The Scripps Research Institute, Division of Virology, Department of Neuropharmacology, 10550 North Torrey Pines Rd., La Jolla, CA 92037. Phone: 858-784-7162. Fax: 858-784-7369. E-mail: bneuman@scripps.edu.

† This is TSRI manuscript 16974-NP.

TABLE 1. PMO and oligonucleotide sequences

Name	Sequence (5'–3')	Positions <sup>a</sup>	Sense <sup>b</sup>
FN-F1	AAGCCAACCAACCTCGATCT	27–46	+
FN-R1	CTTCAGGTGTAGGTTCTGGTTCTGGC	3240–3265	–
FN-R2	CACCGGTCAAGGTCCTACTACCACT	21525–21547	–
FN-R3	GCAGGAGAAGCATTGTCAATTT	25323–25344	–
FN-R4	CAGTAAGGATGGCTAGTGTGACT	26200–26222	–
FN-R5	CATAATCCAGGCTAGGAATAG	26473–26493	–
FN-R6	ATGAAACATCTGTTGTCACTTACT	27059–27082	–
FN-R7	TACCGTCAGCACAAAGCAAAAGC	27462–27483	–
FN-R8	GCGCACCAACAGCTGGATCTTGAC	28006–28029	–
FN-R9	CGTCACCACCACGAACCTCGTCG	28396–28417	–
AUG1	CTTTCGGTCAACCCGGACG	240–259	–
AUG2	GAACAAGGCTCTCCATCTTAC	260–280	–
AUG3	CCAAGAACAAGGCTCTCCATC	264–284	–
TRS1	GTTCGTTTAGAGAACAGATC	53–72	–
TRS2	TAAAGTTCGTTTAGAGAACAG	56–76	–
1ABFS	AAGACGGGCTGCACTTACAC	13408–13427	–
3UTR	GTATCGTAAACGGAATTGCG	29435–29454	–
S2M	GTACTCCGCGTGGCCTCGATG	29587–29607	–
3TERM	TTTTTGTCATTCTCCTAAGAAGC	29710–end	–
DSCR	AGTCTCGACTTGCTACCTCA	N/A <sup>c</sup>	N/A
FT	CTCCCTCATGGTGGCAGTTGA	N/A	N/A
SEQ-F1	TATTAGGTTTTTACCTACCC	2–21	+
SEQ-R2	GAAGAAGAACATTGCGGTATG	614–634	–
RVS-1	CTCCCTCATGGTGGCAGTTGA	1774–1795	–
RVS-2	GAGTTAAATAAAGAGTGTCTG	21637–21657	–
RVS-3	GATTAGCAACTCCTGAAGAGC	26016–26036	–
RVS-4	TTTTTTTTTTGTCATTCTCC	29718–end	–
5UTR-PCRf	ATCGGCTAGCATATTAGGTTTTTACCTACCCAGGAAAAG	2–30	+
5UTR-PCRr	ATCGGTCGACTGACACCAAGAACAAGGCTCTCCATCTTA	262–290	–

<sup>a</sup> SARS-CoV-Tor2, GenBank AY274119.<sup>b</sup> Identical (+) or complementary (–) to the genomic plus-strand.<sup>c</sup> NA, not applicable; non-SARS-CoV sequence.

tary to the AUG translation start site region of a murine coronavirus replicase polyprotein in vitro (29). We reasoned that the activity of P-PMO against coronaviruses might be improved by the rational targeting of RNA sequence elements and secondary structures critical for replication, transcription, and host factor interaction.

In this report, we demonstrate that antisense-mediated suppression of viral replication can be achieved by binding to conserved RNA elements implicated in viral RNA synthesis and translation. Nine P-PMO with sequences complementary to coding and noncoding regions of the SARS-CoV genome were used to probe the function of conserved RNA features during infection in cell culture. The most effective anti-SARS CoV P-PMO described in this report are over 100-fold more active than the anti-murine hepatitis virus coronavirus P-PMO described previously (26). Inhibition of viral yield exceeded 10<sup>4</sup>-fold for compounds designed to bind the transcription regulatory sequence (TRS) region present in the viral genomic 5' untranslated region (UTR). Corresponding effects on viral RNA level, cell-to-cell spread, and cytopathology were observed. Virus clones partially resistant to P-PMO were selected by multiple rounds of growth in the presence of P-PMO. Partially resistant clones selected with a TRS-directed P-PMO developed clustered point mutations at the P-PMO binding site proximal to the leader TRS and grew more slowly in cell culture than wild-type SARS-CoV. We conclude that P-PMO offer a highly specific antisense-based method for probing the

function of specific RNA elements in intact RNA virus genomes in addition to their considerable therapeutic potential.

## MATERIALS AND METHODS

**Cells and viruses.** Vero-E6 cells were cultured in Dulbecco's modified Eagle's medium containing 10% fetal bovine serum, 0.01 M HEPES, penicillin, and streptomycin for general growth and maintenance or in serum-free medium (VP-SFM; Invitrogen) supplemented with L-glutamine, penicillin, and streptomycin during P-PMO studies. SARS-CoV-Tor2 (24) was cultured on Vero-E6 cells. Arenavirus lymphocytic choriomeningitis virus-Armstrong was grown and titrated as previously described (4).

**Plaque assay.** For the SARS-CoV plaque assay, Vero-E6 cells were seeded in 12-well tissue culture plates at  $2 \times 10^5$  cells per well and allowed to adhere overnight at 37°C and 5% CO<sub>2</sub>. The culture medium was removed and replaced with 0.5 ml of inoculum. Cells were treated as specified, and a 2% fetal bovine serum, 0.7% agarose overlay was applied 1 h after inoculation. After 72 h, cells were fixed by immersion in 10% formaldehyde in phosphate-buffered saline for 24 h, agarose plugs were removed, and cells were stained with 0.1% crystal violet. Plaque size reduction assays were cultured and inoculated as above except that individual 0.7% agarose overlays were prepared for each treatment group. Agarose overlays for plaque size reduction assays were prepared with serum-free VP-SFM and P-PMO.

**Virus growth and titer reduction assays.** Vero-E6 cells were seeded at a density of  $5 \times 10^5$  cells per 25-cm<sup>2</sup> tissue culture flask and allowed to adhere overnight at 37°C and 5% CO<sub>2</sub>. Cells were pretreated with 1 ml VP-SFM containing treatment for 6 h, except where stated, as in time-of-addition and time-of-removal experiments. Cells were inoculated with SARS-CoV or lymphocytic choriomeningitis virus Armstrong at a multiplicity of  $\approx 0.1$  or  $\approx 10$  PFU/cell and placed at 37°C for 1 h. The inoculum was removed and replaced with fresh VP-SFM with or without P-PMO treatment. Cell culture medium was collected, stored, and replaced with fresh medium at the designated time points. The virus in cell culture supernatants was titrated by 50% tissue culture infectious dose

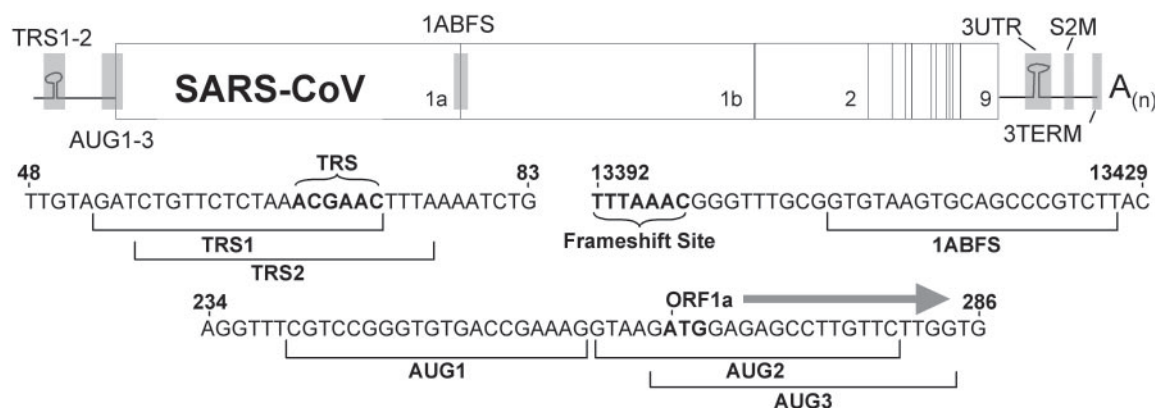


FIG. 1. P-PMO targeting schematic. Relative positions of P-PMO targets on the genomic plus-strand of SARS CoV are indicated by grey boxes. Enlarged regions of the genome indicate the specific target sequences of P-PMO directed against the TRS and AUG regions and the relative proximity of the 1ABFS P-PMO to the ribosomal frameshift site. Nucleotide positions refer to the published sequence of the SARS-CoV-Tor2 strain.

(TCID<sub>50</sub>) with threefold dilution steps analyzed according to the method of Reed and Muench or by plaque assay as described above.

**PMO design, synthesis, and quality control.** PMO were designed to be complementary to the viral plus-strand in several regions showing no sequence variation among sequenced SARS-CoV isolates. Table 1 describes all PMO and DNA oligonucleotide sequences. PMO were synthesized complementary to overlapping sequences in the vicinity of the replicase open reading frame (ORF) 1a initiation codon (AUG1; AUG2; and AUG3), the ORF 1a/1b frameshift signal pseudoknot (1ABFS), the consensus body and leader TRS (TRS1), leader TRS (TRS2), the S2M motif (S2M), the 3'-UTR pseudoknot (3UTR), and the 3' genomic terminus (3TERM; Fig. 1). Random-sequence "nonsense" PMO (DSCR and FT) were included as controls.

PMO targets were screened with BLAST (<http://www.ncbi.nlm.nih.gov/BLAST/>) against known human mRNA sequences in order to preclude unintentional gene-silencing effects. PMO were covalently linked to peptide NH<sub>2</sub>-RRRRRRRFFC-CONH<sub>2</sub> or NH<sub>2</sub>-RRRRRFFRRRRC-CONH<sub>2</sub> designated R<sub>9</sub>F<sub>2</sub> or R<sub>5</sub>F<sub>2</sub>R<sub>4</sub>, respectively. Both types of peptide-conjugated PMO are henceforth referred to as P-PMO. PMO were synthesized at AVI BioPharma Inc. (Corvallis, OR) by a method described previously (38). The conjugation, purification, and analysis of P-PMO compounds were carried out at AVI BioPharma according to methods described elsewhere (25).

**Coiled-coil design, synthesis, and quality control.** We identified a 28-mer peptide from the S2 region of the SARS-CoV spike protein with the highest probability to form a coiled coil using the software program Coils 2.2 (by A. N. Lupas and J. M. Lupas). This peptide, designated SARS-HR2, was synthesized as previously described (18). Circular dichroism (CD) was performed on an Aviv 203-02 spectropolarimeter. Samples for CD contained 10 μM peptide in 5 mM sodium phosphate at pH 5, 6, and 7. Spectra were collected between 200 and 265 nm at 25°C in a 2-mm quartz cell; three spectra were acquired and averaged per sample before subtracting the background spectra.

**Nonviral assays.** The protein-coding sequence for firefly luciferase, without the ATG initiator-Met codon, was subcloned into the multiple cloning site of plasmid pCiNeo (Promega) at the SalI and NotI sites. The pCiNeo expression vector includes both cytomegalovirus and T7 promoters (for mammalian cellular and cell-free transcription of cloned inserts, respectively). Subsequently, complementary oligonucleotides SARS<sub>L</sub><sup>+</sup> and SARS<sub>L</sub><sup>-</sup> were duplexed and subcloned into the NheI and SalI sites. This effectively replaced the start codon of the luciferase gene with sequence encoding bases -31 to +22 relative to the A of the AUG translation start-site codon of the SARS-CoV polyprotein (identical to the region shown in Fig. 1). This leader sequence includes the complete target sites for the AUG1, AUG2, and AUG3 antisense P-PMO. The -31 to +22 target region corresponds to genomic plus-strand nucleotides 235 to 287, as depicted in Fig. 1.

Three other constructs were made in a similar manner by inserting immediately upstream of the intact luciferase gene the DSCR P-PMO target sequence (5'-AGTCTCGACTTGCTACCTCATG-3'), the SARS TRS target sequence that corresponds to nucleotides 51 to 80 of the genomic plus-strand (5'-CTAG ATAGATCTGTTCTCTAAACGAACCTTTAAATG-3'), and the same SARS TRS target sequence that incorporates the three observed nucleotide polymor-

phisms described in the text (5'-CTAGATAGATCTGTTAAATAAACGAACCTTTAAATG-3'). The luciferase gene for each of these three constructs contains a functional ATG initiator-Met codon. A final construct was made by performing PCR with oligonucleotides 5UTR-PCRf (including an NheI site and bases 2 to 30 of genomic plus-strand) and 5UTR-PCRr (including a SalI site and bases 290 to 262 of genomic plus-strand). The resulting 289-bp fragment was restricted with NheI and SalI and subcloned into pCiNeoLuc. This construct utilizes the intact ATG initiator-Met codon within the subcloned SARS sequence (genomic plus-strand bases 266 to 268), as the ATG within the luciferase gene has been deleted.

For the luciferase-fusion constructs that include the TRS sequence, the TRS sequence with three mutations, and the SARS 5'UTR (genomic plus-strand bases 2 to 290), in vitro-transcribed 5'-capped RNA was produced with the mMESSAGE mMACHINE kit (Ambion) after plasmid linearization with NotI. For the SARS AUG and DSCR luciferase fusion constructs, the MegaScript T7 kit (Ambion) was used as described previously (29). In vitro translations were carried out on all constructs as described previously (29). Luciferase-induced light emission was read on a FLx800 microplate luminometer as described previously (29). Cellular efficacy studies were carried out using confluent Vero-E6 cells transiently transfected with target-leader/luciferase plasmids using Lipofectamine (Gibco BRL) according to the manufacturer's directions and assayed as above. The 3-(4,5-dimethylthiazol-2-yl)-2,5-diphenyl tetrazolium bromide (MTT) assay was used to measure cell viability as described previously (29).

**Resistance studies.** Virus was passaged 11 times on fresh Vero-E6 cells pretreated with 2 to 10 μM P-PMO. Biologically cloned viruses were cultured from individual, well-spaced plaques. Viral RNA was prepared from infected cells by Trizol lysis followed by an additional chloroform extraction. Reverse transcription-PCR was carried out according to the enzyme manufacturer's specifications (Invitrogen). The 5'-terminal region of the SARS-CoV genome was amplified using primers SEQ-F1 and SEQ-R2. PCR products were sequenced using primer SEQ-R2. Relative RNA load was determined by 25-cycle PCR of cDNA primed with oligonucleotides RVS1 through RVS4. PCR was primed with FN-F1 and the appropriate FN-R oligonucleotide to generate products of 104, 127, 156, 188, 212, 259, 299, and 353 bp, corresponding to viral subgenomic RNAs 2 through 9, respectively.

## RESULTS

**Design of antivirals.** P-PMO were designed to target conserved viral sequences implicated in SARS-CoV RNA synthesis, translation, and/or host factor interaction (Fig. 1). The expression of the coronavirus replicase polyprotein is controlled at two points: the initiation of translation at open reading frame 1a, and the ribosomal frameshift which results in translation of the extended open reading frame 1ab. Three sequences were selected in the immediate vicinity of the AUG translation-initiation codon of the viral replicase polyprotein

open reading frame 1a (AUG1, AUG2, and AUG3) such that AUG2 and AUG3 overlapped the initiation codon and AUG1 was located in the 5' untranslated region proximal to the translation start site. P-PMO 1ABFS was designed to disrupt the RNA secondary structure at the -1 ribosomal frameshift site that mediates translation of the remainder of the replicase polyprotein. The untranslated 5'-terminal 263 nucleotides of the SARS-CoV RNA also contain the  $\approx 80$ -nucleotide leader sequence found at one terminus of each of the 5'- and 3'-coterminal subgenomic viral RNA species produced in the infected cell.

The transcription regulatory sequence (TRS) located in the 5'-UTR of the genome is believed to participate in discontinuous RNA synthesis (30–32, 39). The leader TRS was targeted with two P-PMO, each designed to mask the consensus TRS (5'-CGAAC-3') and disrupt the stem-loop predicted to form in this region (40). TRS1 is complementary to the TRS in the leader RNA present on both genomic and subgenomic RNA species. TRS2 spans the junction between the leader and a portion of the 5'-UTR not present on subgenomic RNAs (39).

Studies of coronavirus defective-interfering RNAs have shown the genomic termini contain several conserved motifs, some of which act as discrete signals for RNA replication (6, 15). P-PMO compounds designed against targets in the 3'-untranslated region included 3UTR, targeting a portion of the conserved RNA stem-loop/pseudoknot found in most coronavirus genomes (10–13); S2M, targeting the stem-loop 2 motif region related to sequences in astroviruses and equine rhinovirus (17); and 3TERM, targeting the 3' terminus of the genomic RNA, including the first five bases of the polyadenosine tail. Two nonsense P-PMO, DSCR and FT, were included to control for nonspecific P-PMO effects. The 5' termini of P-PMO were conjugated to an arginine-rich delivery peptide ( $R_9F_2$ ; 26, 29) or to a rearranged  $R_5F_2R_4$  peptide, which confers equivalent delivery and efficacy properties (Moulton et al., unpublished data). The  $R_9F_2$  and  $R_5F_2R_4$  peptide conjugates were used interchangeably in the antiviral studies presented here. We did not observe detectable differences in sequence-specific or nonspecific effects between PMO conjugated to one or the other of the two delivery peptides.

Non-antisense antiviral compounds which targeted different stages of the viral growth cycle were included in some assays to provide a bridge for comparison of the results reported here with other studies reported in the literature. Among the control antivirals tested was a peptide identical to the carboxyl-terminal heptad repeat region of the SARS-CoV spike (HR2), which was designed to bind the spike protein during virus-cell fusion and arrest fusion at an intermediate stage. Amphipathic helices of the SARS and murine hepatitis virus coronaviruses form six-helix bundles that are believed to mimic the postfusion state of the spike glycoprotein. Several reports have demonstrated the antiviral properties of peptides based on amphipathic helices of coronavirus spike protein (3, 14, 22, 47).

We synthesized and purified a heptad repeat peptide derived from residues 1158 to 1185 of the SARS-CoV-Tor2 spike protein, designated SARS-HR2. The SARS-HR2 protein was selected to allow comparison of direct inhibition of SARS-CoV growth by different methods, e.g., fusion arrest versus antisense. The circular dichroism spectrum of SARS-HR2 (data not shown) displayed an equilibrium between disordered and

helical structure, as previously reported for similar peptides (14).

**P-PMO are effective and specific.** As we have reported previously, the conjugated "delivery" peptides increase both the efficacy and toxicity of PMO in cell culture (29).  $R_5F_2R_4$ -conjugated PMO were tested for cytotoxicity by the MTT assay under the serum-free culture conditions used throughout this report.  $R_5F_2R_4$ -PMOs were nontoxic (defined as  $\geq 90\%$  cell viability after 24 h) at concentrations as high as 20  $\mu$ M on Vero-E6 cells (data not shown). The level of toxicity of  $R_5F_2R_4$ -PMO was similar to that reported for  $R_9F_2$ -PMO previously (29). Based on this finding, treatment doses of P-PMO were limited to 20  $\mu$ M. Hygromycin B, a broad-spectrum translation inhibitor active against most coronaviruses, was nontoxic to  $\geq 80 \mu$ M (data not shown), in agreement with other published results (2).

P-PMO designed to inhibit initiation of translation of the SARS-CoV replicase polyprotein were tested in a rabbit reticulocyte lysate cell-free translation assay to determine which compound was most effective at inhibiting expression of a luciferase reporter. P-PMO were added to reticulocyte lysates programmed with in vitro-transcribed RNA in which translation of the luciferase gene was initiated at a small region derived from the SARS-CoV 5'-UTR containing the AUG1-3 P-PMO target sites. AUG1, AUG2, and AUG3 P-PMO generated comparable nanomolar-scale dose-dependent reduction of luciferase expression in this cell-free translation system (Fig. 2A). The FT P-PMO, described in our previous studies (29), was included here as a negative control.

DSCR P-PMO consistently generated low nonspecific activity in a variety of assays in this study. In order to demonstrate that the ineffectiveness of DSCR was not due to some innate defect in the compound itself, we compared the effects of DSCR and AUG1 P-PMO on inhibition of luciferase expression from a DSCR-target/luciferase construct (Fig. 2B). As expected, DSCR P-PMO specifically suppressed translation from the DSCR/luciferase transcripts. Nonspecific effects of AUG1 P-PMO against the DSCR/luciferase RNA were comparable to those of DSCR P-PMO against the SARS AUG-target/luciferase RNA described above. We therefore concluded that the DSCR and P-PMO AUG1 to AUG3 acted solely through antisense activity and displayed low nonspecific effects.

The three AUG P-PMO also displayed equivalent micromolar-scale effects on translation of the reporter gene in Vero cell cultures transiently transfected with the SARS/luciferase reporter plasmid used in the previous experiment (Fig. 2C). Synergistic effects can potentially be obtained when antiviral compounds with different targets are administered in combination (41). Nonoverlapping combinations of P-PMO were tested in the cell-free translation system in order to screen for additive synergy or anergy. The effects of combinations of AUG1 to AUG3 at a given total molarity did not differ significantly from the effects of an individual AUG P-PMO at the same total molarity (Fig. 2C), as might be expected for compounds targeting essentially identical targets by the same mechanism.

**Reduction of SARS-CoV CPE and growth.** In order to characterize the nine SARS-CoV-specific P-PMO, we tested them for several correlates of antiviral efficacy: prevention of cyto-



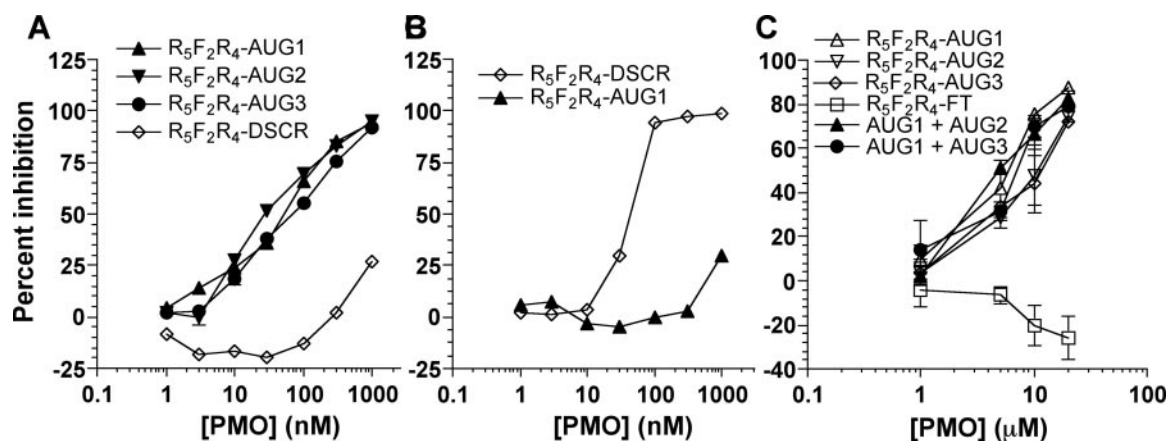


FIG. 2. Peptide-conjugated PMO specifically reduce cell-free and cell culture expression of plasmid-generated target sequences. (A) Cell-free translation assay demonstrates the inhibition of SARS AUG region/luciferase translation by AUG P-PMO relative to nonspecific activity of the DSCR control P-PMO. Data are expressed as percent inhibition relative to 12 untreated control values. (B) The converse assay, inhibiting translation from DSCR target/luciferase RNA specifically with the DSCR P-PMO demonstrates the lack of cross-reactivity of DSCR and AUG P-PMO in this system. (C) Luciferase expression from AUG region/luciferase mRNA generated from a transiently transfected plasmid in cell culture was inhibited by single-AUG P-PMO and combination AUG PMO treatments. Concentrations of combined P-PMO are expressed as the molarity of a 1:1 mixture of two nonoverlapping compounds. Error bars indicate standard error of the mean.

pathic effects, reduction of viral titer, and reduction of the spread of an established infection. SARS-CoV cytopathic effects (CPE) on Vero-E6 include vacuolation and extensive cell rounding by 24 h postinoculation in the case of high-multiplicity inoculation. We chose to compare cytopathic effects 72 h after high-multiplicity ( $\geq 10$  PFU/cell) inoculation, by which time cells in untreated controls and those receiving ineffective treatments had displayed severe CPE for 24 to 48 h (Fig. 3A). Typical SARS-CoV-induced CPE was observed in infected cells treated with vehicle (water) only, DSCR, S2M, and 3TERM-P-PMO. The AUG1, AUG2, AUG3, 1ABFS, and 3UTR P-PMO consistently reduced CPE only after 20  $\mu$ M treatment (AUG1 results are presented in Fig. 3A; the remaining data are not shown). Treatment with lower doses of AUG1 to AUG3 P-PMO appeared to reduce the severity of CPE in some experiments, as in the case shown in Fig. 3A. However, the protective effect of lower doses of the three AUG-targeted P-PMO was not observed consistently, and when present was always less pronounced than the protective effect of either TRS-targeted P-PMO. TRS1 and TRS2 strongly reduced CPE after  $\geq 6$   $\mu$ M treatment (results for TRS1 are presented in Fig. 3A; TRS2 data are not shown). We thus concluded that TRS1 and TRS2 had at least a threefold greater antiviral activity compared to the AUG1 to AUG3, 1ABFS, or 3UTR P-PMO. The AUG3 P-PMO was not studied further since it was not found to differ from AUG2 or AUG1 in efficacy, toxicity, or CPE reduction.

Next, P-PMO were tested for the ability to reduce virus yield in pretreated cells. It is our observation that SARS-CoV growth plateaus by 24 h and remains high through 48 h following high-multiplicity inoculation ( $\geq 3$  PFU/cell) or peaks  $\approx 24$  h later following low-multiplicity inoculation ( $\leq 0.1$  PFU/cell). In order to compare P-PMO effects on log-phase viral growth, we compared infectious titers 24 h after low-multiplicity inoculation (Fig. 3B). The viral titer results were generally consistent with the cytoprotection results (Fig. 3A). The most effective P-PMO decreased viral titers to below the threshold

of detection, 100 PFU/ml in the experiment shown in Fig. 3B. The 3UTR P-PMO had slight antiviral effects, while 1ABFS, AUG1, and AUG2 displayed equivalent moderate antiviral activity. TRS1 and TRS2 clearly exhibited robust antiviral activity in the low micromolar range. In repeated experiments, titers were consistently reduced by over 100-fold by treatment with  $\geq 6$   $\mu$ M AUG1, AUG2 and 1ABFS P-PMO or by  $\geq 2$   $\mu$ M TRS1 and TRS2 PMO.

We next sought to further characterize the highly effective TRS2 P-PMO by performing time course studies in which this compound was added or removed at different times. Antivirals affecting a particular stage of the viral growth cycle, such as entry (early) or assembly (late), would likely be effective on different time scales, whereas inhibitors of ongoing processes such as replication and translation could be active at any point prior to the peak of viral growth. In order to investigate this hypothesis, we tested the effects of time of addition on the control heptad repeat peptide SARS-HR2, designed to inhibit virus-cell fusion after receptor binding and some conformational changes have occurred. SARS-HR2 was active when administered 1 h before inoculation or in combination with the inoculum. SARS-HR2 did not alter the titer of infectious virus present in the supernatant 24 h postinoculation when SARS-HR2 was administered 1 h postinoculation or later, indicating that an early event was targeted, and consistent with the predicted target of the membrane fusion process (data not shown). The TRS2 P-PMO significantly reduced viral titer when added up to 4 h after high-multiplicity infection and 8 h after low-multiplicity infection (data not shown), consistent with the effects expected from inhibition at a later stage in the viral life cycle. However, this result also indicated a requirement that TRS2 P-PMO be present early in the infection process for maximal antiviral effect.

In order to determine the duration and reversibility of TRS2 P-PMO-mediated antiviral effects, the TRS2 P-PMO was removed from the cell culture medium at various intervals and viral titer was assessed at several time points (Fig. 3C). Re-

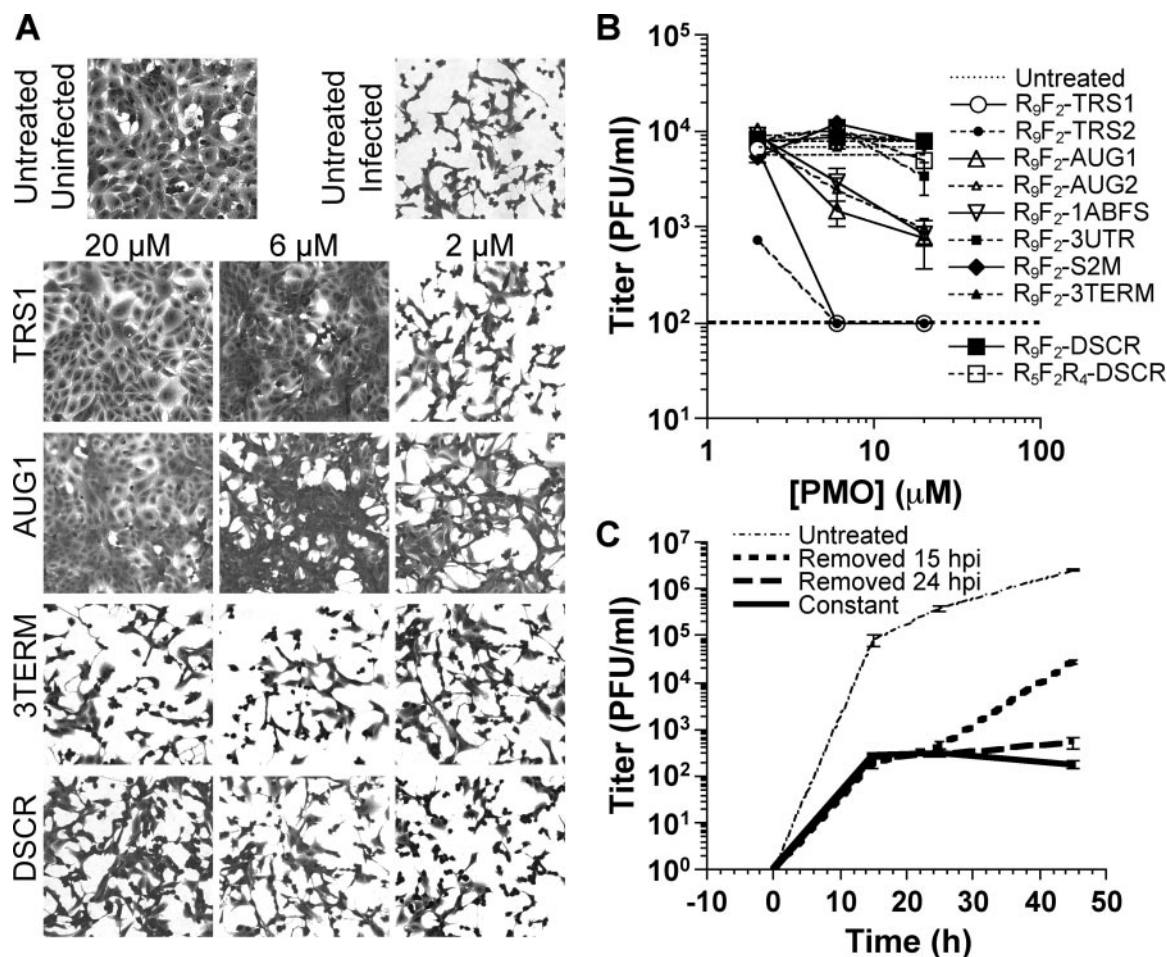


FIG. 3. Peptide-conjugated PMO reduce SARS-CoV cytopathology and titer. Qualitative changes in cell morphology and density were gauged against untreated infected (upper right) and untreated uninfected (upper left) controls. (A) Representative images of cells pretreated for 6 h with selected  $R_9F_2$ -conjugated PMO and fixed 72 h after inoculation. (B) Dose-response of titer reduction. Triplicate wells of Vero-E6 cells were pretreated with P-PMO or vehicle-only at 6 h before inoculation with SARS-CoV at a multiplicity of 0.1 PFU/cell. Virus yield was quantified 24 h after. The limit of detection for the assay shown was 100 PFU/ml. Error bars indicate standard error of the mean. (C) Cells were pretreated with 20  $\mu$ M TRS2  $R_9F_2$ -PMO or mock treated 6 h before inoculation. Culture medium was collected at 15 h and 24 h and replaced with medium containing P-PMO or medium alone as indicated. Virus yield was measured at 15 h, 24 h, and 48 h.

removal of TRS2 P-PMO as late as 15 h after infection resulted in increased viral amplification as measured at 24 and 48 h. This result suggests either rapid neutralization of the P-PMO or saturation of the TRS2 P-PMO molecules at the site of activity for a period of time. Taken together, these results demonstrate that the constant presence of TRS2 P-PMO is required to maintain maximum antiviral activity.

**Preventing spread of an existing infection.** Pathways leading to the establishment or spread of an infection can differ for some viruses. In murine hepatitis virus, initial cell entry of virus has rigorous receptor specificity requirements, but infection can subsequently be spread to receptor-null cells by contact with infected cells (8). Consequently, despite the positive results for the AUG1 to AUG3, 1ABFS, and TRS1 and TRS2 P-PMO, we hypothesized that successful inhibition of SARS-CoV-induced CPE and infectious titer might not necessarily predict effective treatment of an existing infection. The effects on viral persistence and spread of an existing infection were measured in a plaque size reduction assay. In this assay, cells

were treated with P-PMO 1 h after inoculation with a standardized amount of SARS-CoV. The progress of the initial infection was quantified by measuring the diameter of the resulting viral plaques 72 h after inoculation.

The observed effects on viral spread (Fig. 4A-C) closely resembled the titer reduction results (Fig. 3B). DSCR, 3UTR, S2M, and 3TERM P-PMO were ineffective. The dose-response curves of the AUG1 and AUG2 P-PMO were essentially equivalent and showed slightly more potency than the 1ABFS P-PMO. The TRS1 and TRS2 P-PMO were again the most effective. Treatment with  $\geq 6$   $\mu$ M TRS1 or TRS2 P-PMO completely prevented the formation of visible plaques.

We compared the effects of the AUG1 P-PMO against DSCR P-PMO, SARS-HR2 peptide, and hygromycin B on the spread of SARS-CoV infection (Fig. 4C). The slopes of the dose-response curves for hygromycin B and the AUG1 P-PMO were similar, indicating similar kinetics of activity, although the AUG1 P-PMO was approximately 10-fold more potent than hygromycin B. The slope of the dose-response curve for SARS-

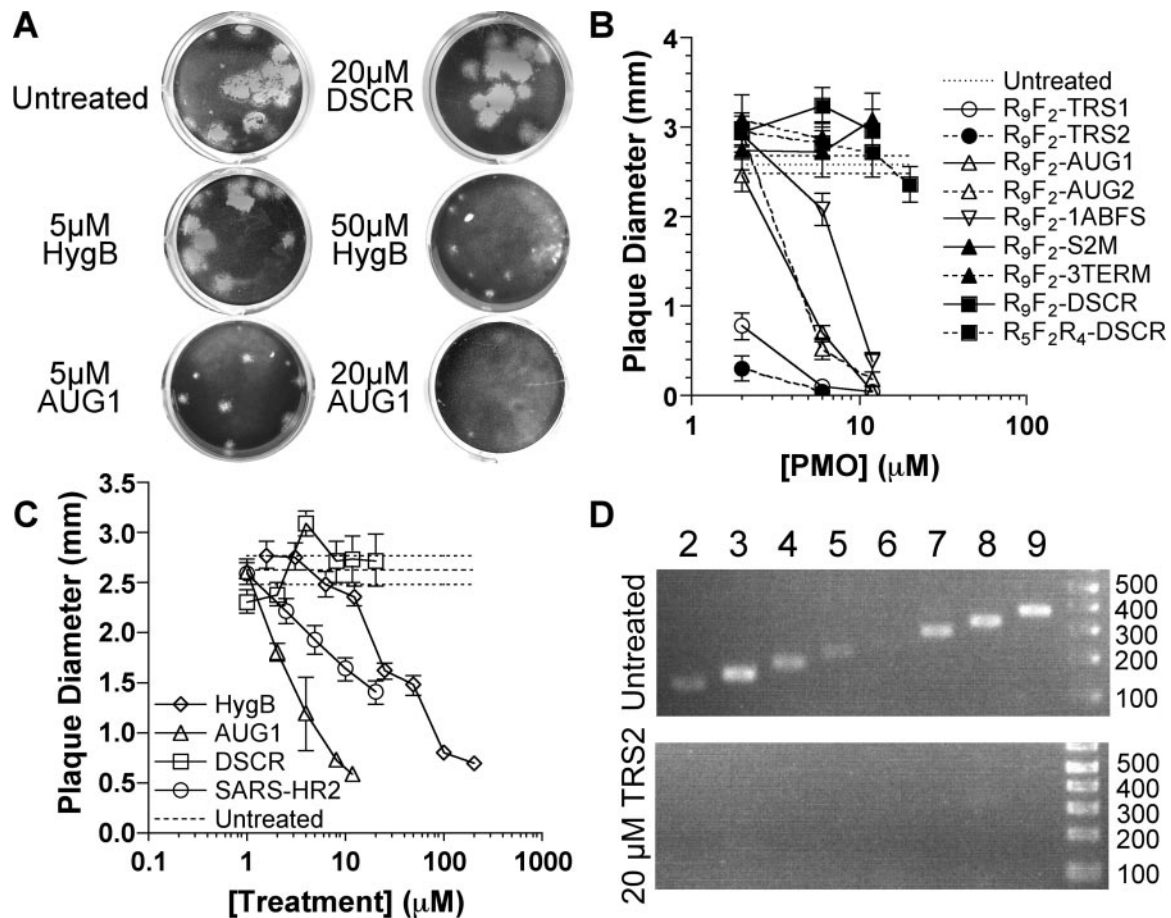


FIG. 4. Peptide-conjugated PMO and coiled-coil peptides inhibit the propagation of SARS-CoV infection. Plaque diameter on treated and mock-treated cells was visualized (A) and measured (B) 72 h after inoculation under the same experimental conditions as described for Fig. 3A. (C) Comparison of 72-h plaque diameter on cells treated with  $R_5F_2R_4$ -AUG1 P-PMO,  $R_5F_2R_4$ -DSCR P-PMO, hygromycin B (HygB), or coiled-coil SARS-HR2 and on mock-treated cells (untreated). Error bars indicate standard error of the mean. (D) Reverse transcription-25-cycle PCR comparison of viral subgenomic RNA 2 to 9 levels in an equivalent number of mock-treated or 20  $\mu$ M TRS2 P-PMO-treated cells 24 h after inoculation. Sizes in bp are indicated to the right. Amplicons of 104, 127, 156, 188, 212, 259, 299, and 353 bp were expected, corresponding to viral subgenomic RNAs 2 through 9, respectively.

HR2 was less steep, indicating that relatively more SARS-HR2 was required to produce incremental inhibitory effects compared to P-PMO or hygromycin B. Possible explanations for this difference in dose-response ratio include peptide lability, the brief availability of the transition state amenable to competitive SARS-HR2 binding during the fusion process compared to continuous inhibition by hygromycin B or P-PMO, and the potential for up to three SARS-HR2 peptides to bind each prefusion intermediate of the spike homotrimer compared to the presumed binding of one P-PMO molecule per viral RNA molecule.

We reasoned that the observed inhibition of viral growth and propagation might correspond to a decrease in the viral RNA level, whether through inhibition of replicase expression, interference with discontinuous RNA synthesis at the leader TRS, or an alternative mechanism. Coronaviruses produce a nested set of subgenome-length RNA species in infected cells. Most coronavirus subgenomic RNAs are produced in molar excess of the genomic RNA, though genomic RNA and trace amounts of subgenomic RNAs are typically packaged in the

virion (reviewed in reference 33). Therefore, we investigated genomic and subgenomic RNA production 24 h after low-multiplicity inoculation, as an indicator of ongoing infection. The 24-h time point was selected as a time when several rounds of replication would have occurred but virus-induced cell lysis would be negligible.

Reverse transcription-PCR products specific for each of eight subgenomic RNA species were strongly amplified from mock-treated cells and cells treated with mildly effective P-PMO (Fig. 4D and data not shown). Equal volumes of reverse transcription-PCR products from an equivalent number of 20  $\mu$ M TRS2 P-PMO-treated cells were faint (i.e., subgenomic RNA 8 and possibly 9) or undetectable (subgenomic RNAs 2 to 7; Fig. 4D). Genomic RNA synthesis was likewise qualitatively reduced by 20  $\mu$ M TRS2 P-PMO (data not shown), though whether this resulted directly from steric hindrance of target RNA or indirectly through inhibition of replicase polypeptide expression was not determined. This result suggests P-PMO effects on SARS-CoV growth, CPE, and spread correlate with a qualitative decrease of viral RNA level.



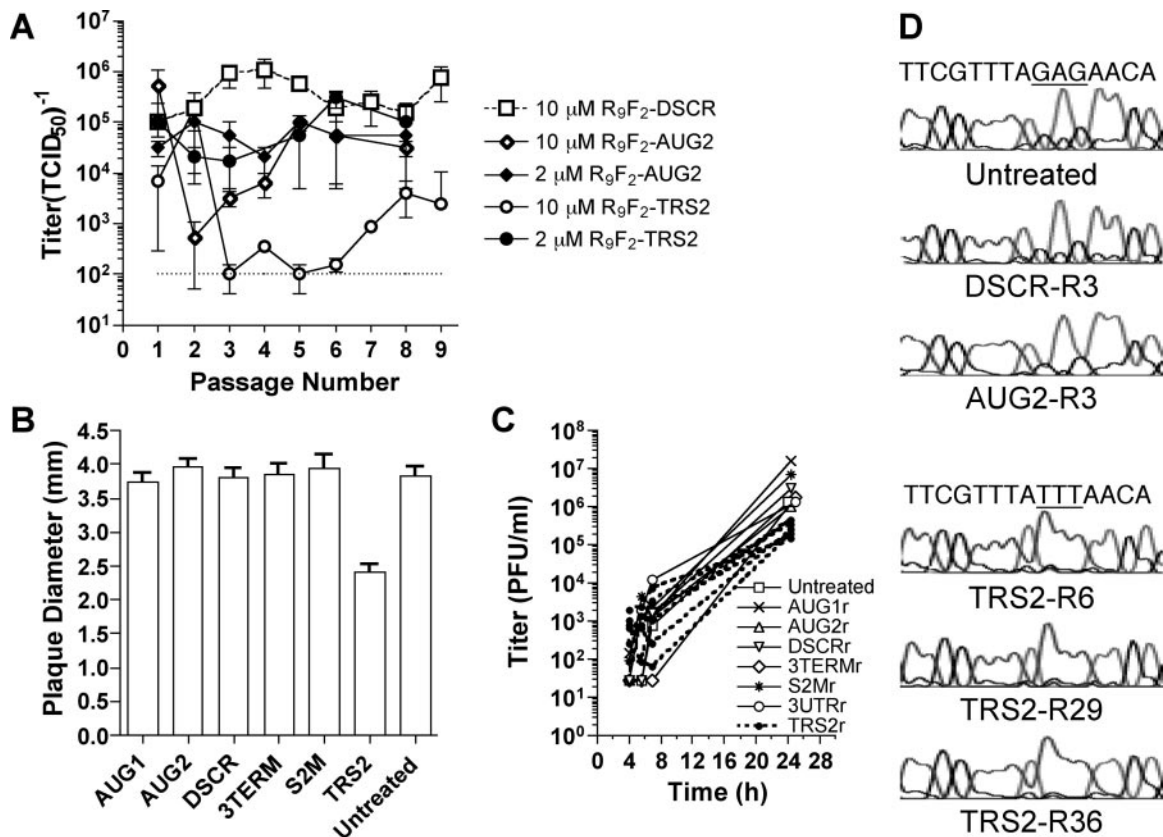


FIG. 5. Characterization of P-PMO-resistant SARS-CoV. SARS-CoV was serially passaged on cells pretreated with 2  $\mu$ M or 10  $\mu$ M R<sub>9</sub>F<sub>2</sub>-PMO or mock-treated cells. (A) Virus yield over the first nine passages was quantified 24 h after inoculation at an initial multiplicity of  $\approx 10$  PFU/cell. (B) The diameters of 50 plaques were measured after 11 viral passages on untreated or 10  $\mu$ M P-PMO-treated cells. (C) Growth kinetics of P-PMO-resistant plaque-purified SARS-CoV on untreated Vero-E6 cells are shown. Biologically cloned virus was cultured from plaque-purified stocks selected after 11 passages on untreated cells or cells treated with AUG1, AUG2, S2M, 3TERM, 3UTR, TRS2, or DSCR P-PMO. Growth curves for five median-growth partially TRS2-resistant SARS-CoV biological clones are shown. TCID<sub>50</sub> titrations were calculated for four fourfold replicates. Error bars indicate standard error of the mean. (D) The 5'-terminal regions of P-PMO-resistant and mock-treated clones were amplified and sequenced in the antigenomic orientation. A portion of the TRS2 P-PMO target region is shown, with the mutations in TRS2-resistant clones underlined.

**Specificity of P-PMO.** The most effective anti-SARS-CoV P-PMO was found to be TRS2. Therefore TRS2 was tested for effects on an unrelated virus, the arenavirus lymphocytic choriomeningitis virus, that grows well in Vero-E6 cells under the same culture conditions under which the SARS-CoV experiments were carried out. Cells treated with 2 to 20  $\mu$ M TRS2 were inoculated at a multiplicity of about 0.1 PFU/cell, and cell culture supernatants were harvested and titrated by plaque assay. Virus amplification at 24 h was not significantly altered in cells treated for 6 h with TRS2 P-PMO at any concentration compared to untreated controls (data not shown). Although the cellular functions required for arenavirus and coronavirus replication are likely not identical, we interpret this result as a further confirmation that the effectiveness of P-PMO against SARS-CoV was antisense mediated.

**Partial resistance to P-PMO.** The error-prone replication of RNA viruses presents a rapid model for viral evolution and drug resistance studies. In order to assess the propensity for SARS-CoV to develop resistance to antisense P-PMO, a stock cultured from a plaque-purified biological clone of SARS-CoV was serially passaged on cells treated with 0.5, 2, or 10  $\mu$ M

P-PMO. The term biological clone as used here designates an isolate derived from a single viral plaque. We chose to administer submaximal doses of P-PMO in order to allow the generation of P-PMO-resistant mutant strains. SARS-CoV was passaged blindly 11 times in cells pretreated with P-PMO. Viral growth was assessed, as an indicator of resistance, after each of the first nine passages (Fig. 5A).

The 3TERM and DSCR P-PMO did not inhibit SARS-CoV growth at any concentration or passage number. The AUG1, AUG2, and 3UTR P-PMO inhibited SARS-CoV growth for one to three passages after 10  $\mu$ M treatment only. Treatment with 10  $\mu$ M TRS2 P-PMO strongly inhibited SARS-CoV growth in each of the 11 passages tested. However, an increase in titer indicative of partial resistance was observed by passage 7. The peak titer of the TRS2 P-PMO-resistant virus population, during the 11 passages performed, was at least 100-fold below the titer of mock-treated cells, indicating acquisition of partial but not total resistance.

Viral plaques reflect the progress of a single infected cell's progression through multiple waves of viral entry, replication, and spread, and altered plaque diameter or morphology can be



indicative of perturbation to some stage of the virus replication cycle. To determine whether partially or totally P-PMO-resistant virus clones displayed altered amplification characteristics in the absence of P-PMO selection, plaque morphology and size were examined (Fig. 5B). Plaque morphology was found to be unaffected, though TRS2-selected biological clones displayed a smaller plaque morphology compared to that of wild-type SARS-CoV. Eight to 41 plaque-purified viruses were selected from each treatment pool. All AUG1, AUG2, DSCR, 3UTR, S2M, and 3TERM P-PMO-selected viruses caused typical CPE on Vero-E6 cells. Sixteen of 41 TRS2 P-PMO-selected clones caused negligible CPE on cells 72 h after inoculation, while the remaining clones caused reduced CPE.

One-step growth curves were performed for a selection of the P-PMO-selected SARS-CoV biological clones. TRS2 P-PMO-selected clones displayed delayed growth kinetics compared to untreated SARS-CoV and other P-PMO-selected clones (Fig. 5C). The titers of untreated and non-TRS P-PMO-treated SARS-CoV biological clones displayed in Fig. 5C represent typical titers observed 24 h after high-multiplicity inoculation. Continuous TRS2 P-PMO treatment, as shown in Fig. 3C, suppressed viral titers to approximately 100 PFU/ml, a decrease of  $\approx 4$  to 5  $\log_{10}$  from peak titers of  $\approx 6$  to 7  $\log_{10}$  observed in Fig. 3C, 5A, and 5C.

Reverse transcription-PCR amplicons from 14 TRS2-P-PMO-resistant SARS-CoV clones and one each of AUG1, AUG2, DSCR, 3UTR, S2M, and 3TERM and mock-treated clones were sequenced to determine whether the observed phenotypes correlated with specific genetic variations (Fig. 5D). Three consensus sequences were obtained for each biological clone, reflecting the dominant genotype over the first  $\approx 600$  bases proximal to the 5' terminus of the genomic plus-strand. The sequences fell into two categories: TRS2-resistant clones each carried an identical set of mutations. Clones resulting from selection with the other P-PMO and mock treatment-selected clones were all identical. The 21 sequences that were obtained differed at three points: a silent mutation, C543T, and a block of three contiguous base changes of CTC to AAA at positions 62 to 64 proximal to the leader TRS (within the target region of TRS2-P-PMO) appeared in only the 14 TRS2-resistant clones, whereas a mutation, T281C, resulting in a leucine-to-proline shift at the sixth codon of ORF1a was present in only the AUG1, AUG2, DSCR, 3UTR, S2M, and 3TERM P-PMO-selected and vehicle-treated clones. Since the point mutation at position 281 relative to the original SARS-Tor2 sequence was found in both selected and mock-selected clones, we interpret this change as having likely evolved during serial passage in Vero-E6 cells prior to P-PMO selection. All TRS2-resistant clones identified likely derived from a single escape mutant. Mutations were not observed in the AUG1 or AUG2 P-PMO target regions of clones resistant to either of these P-PMO. We cannot at present rule out the possibility of compensating downstream mutations in AUG P-PMO-resistant biological clones.

Thermal melting curve data for peptide-conjugated PMO/RNA duplexes with variable mismatches led us to speculate that the three mutations at the TRS2-P-PMO target site reduce the effective binding affinity as measured by melting temperature ( $T_m$ ) by  $\approx 25$  to  $30^\circ\text{C}$  (H. Moulton et al., manuscript in preparation) (36). We are unable at present to predict the

precise number of mutations required to completely abrogate P-PMO efficacy. However, we tested the hypothesis that decreased affinity of the TRS2 P-PMO for the mutated target site could explain the decreased sensitivity of TRS2-selected SARS-CoV biological clones to TRS2 P-PMO.

P-PMO binding affinity was compared using a reporter construct in which the luciferase reporter gene was placed immediately downstream of either the wild-type SARS-CoV TRS region or the same region with the CTC $\rightarrow$ AAA mutations observed in TRS2 P-PMO-selected SARS-CoV clones (Fig. 6A). TRS2 P-PMO was approximately 10-fold less active against the three-mismatch TRS target compared to the wild-type target ( $\text{EC}_{50}$  of 500 nM and 50 nM, respectively).  $\text{EC}_{50}$ , as used here, refers to the amount of compound required to reduce luciferase luminescence by 50% compared to untreated controls. The decreased TRS2 P-PMO sensitivity of TRS2-selected strains was therefore consistent with the apparent reduction in stability of the P-PMO/target RNA duplex in TRS2-resistant biological clones. A similar observation was recently reported for human immunodeficiency virus type 1 escape variants resistant to small interfering RNAs (43).

While the experiments described above addressed the specificity and efficacy of P-PMO, we also wished to explore which molecular events of the viral life cycle the TRS2 P-PMO was affecting. In order to examine the effects of TRS2 PMO on inhibition of viral translation, a luciferase reporter construct was designed in which the entire SARS-CoV 5'-UTR was placed upstream of the reporter. The new reporter construct was designed so that luciferase expression would be initiated at the authentic SARS-CoV ORF 1a AUG codon. Contrary to our expectation, the TRS2 P-PMO outperformed AUG1 P-PMO by severalfold in translation inhibition ( $\text{EC}_{50}$ s of 35 nM and 185 nM, respectively; Fig. 6B). The TRS2 target site (bases 55 to 75) is sufficiently distant from both the 5' terminus and the site of translation initiation to make it unlikely that interference with any of the discrete events of preinitiation at the terminus (e.g., 43S complex loading onto mRNA) or initiation at the initiator AUG (e.g., 48S-complex formation and/or joining of 48S and 60S ribosomal subunits) forms the basis for the observed effect. We therefore concluded, pending further testing, that TRS2 P-PMO inhibits SARS-CoV amplification primarily by interfering with the 43S preinitiation complex scanning process.

## DISCUSSION

The results of this study demonstrate that P-PMO specific to the SARS-CoV genome can reduce production of infectious virus and thereby protect cells from virus-induced CPE as well as slow the cell-to-cell spread of infection. P-PMO acted by a sequence-specific mechanism, with low nonspecific activity on off-target cellular and viral functions. SARS-CoV overcame the antiviral activity of P-PMO directed against a number of sites on the viral genome, while resistance to P-PMO targeting the leader TRS element developed only after several host cell passages. The precise mechanism and timing of TRS2-associated nucleotide changes is unclear. We note, however, that the 5'-UTR typically displays relatively low sequence variability among coronaviruses of one species (one notable exception being a TRS-proximal polymorphism in murine hepatitis virus

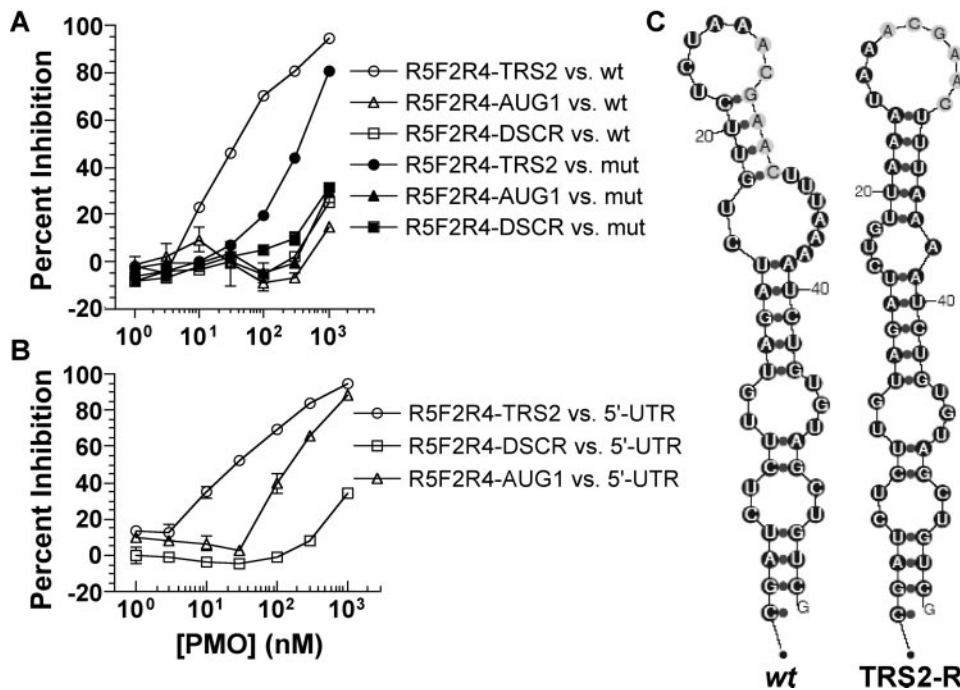


FIG. 6. Mechanisms of P-PMO efficacy and partial resistance. (A) Binding of P-PMO to the TRS region (nucleotide positions 51 to 79) was assessed in a cell-free translation inhibition assay. The relative binding strength of P-PMO to the wild-type SARS-CoV target (wt) and the three-mispair target (mut) is expressed as percent inhibition of luciferase expression. Zero percent inhibition was determined by the average level of luciferase expression from untreated control translations programmed with both wild-type and mutant mRNAs. (B) Comparison of inhibition of luciferase expression downstream of the entire SARS-CoV 5'-UTR sequence by three P-PMO. Error bars indicate standard error of the mean. (C) Low-energy secondary structures of the TRS hairpin of wild-type SARS-CoV (wt) and TRS2 P-PMO-selected SARS-CoV (TRS2-R) were generated using Mfold (49). The core TRS is near the top of the stem and shown in white circles; flanking sequences are depicted inside black circles. Nucleotides are numbered from the beginning of the predicted stem-loop.

JHM) (46), and the observed TRS2-associated polymorphism is not represented among SARS-CoV sequences currently available in the GenBank database. SARS-CoV resistant to TRS P-PMO displayed reduced cytopathology and cell-to-cell spread. Mutations at the TRS 2 P-PMO target site confirm that P-PMO act directly on the viral RNA, as similarly shown for in situ-generated RNA complementary to human immunodeficiency virus type 1 *env* (23) and small interfering RNAs directed against human immunodeficiency virus type 1 (43). Decreased P-PMO-target affinity to altered target sequence almost certainly explains the observed loss of P-PMO sensitivity in resistant isolates.

The CTC→AAA mutations found in all TRS2-P-PMO-resistant SARS-CoV clones occur outside the region occupied by the consensus TRS (5'-CGAAC-3') (Fig. 6C), but within the TRS2 P-PMO target region. No mutations were observed in resistant isolates cloned from cultures treated with other P-PMO. The presence of short complementary regions surrounding the TRS is a conserved feature among the *Nidovirales* and is called stem-loop II (5) or the leader TRS hairpin (40). Mfold secondary-structure predictions (49) indicate that the TRS2-resistant SARS-CoV could form a destabilized alternate hairpin conformation (boldface), **TTAAA-TAAACGAAC-TTAA**, surrounding the TRS (italic). The lowest-energy fold of the TRS hairpin with the AAA mutation has a calculated  $\Delta G$  of  $-4.1$  kcal/mol, compared to  $-7.0$  kcal/mol for the wild-type CTC sequence.

Our analysis yields no compelling rationale that would favor the incorporation of the particular set of mutations observed. Finding a clustered three-nucleotide substitution in a coronavirus after 11 passages would generally be considered a rare event, and further study will be required to clarify the mechanism involved. Moreover, it is unclear whether these point mutations arose from a low-probability chance event or whether the particular set of mutations observed represent a preferred solution to the selective pressures toward optimal replication and drug resistance. So, while it would appear that antisense may designate a site for mutation, the present data are insufficient to suggest the type of mutation most likely to be incorporated.

Levels of P-PMO efficacy appeared to group with respect to the nature of the viral target sequence. This was most striking in the case of the AUG1 P-PMO, targeted to the 3' end of the 5'-UTR, the AUG2 and AUG3 P-PMO, which directly masked the ORF 1a translation initiation codon, and the 1ABFS P-PMO, targeted over 13 kb downstream. All four of these P-PMO were conceived as inhibitors of replicase translation, with targets designed to interfere with ribosome scanning, translation initiation, or the ribosomal frameshift event by which the coronaviruses produce the enzymatic products of ORFs 1a and 1b. Results for the 3UTR P-PMO, though modest, were interesting because the effects of 3UTR cannot be readily attributed to inhibition of translation and therefore likely derive from some effect on viral RNA synthesis. The selection of the 3UTR

P-PMO target was perhaps unfortunate, as a study from the Masters group that appeared during the course of our studies showed that the loop and upper stem regions of the stem-loop/pseudoknot structure in the 3'-UTR targeted by the 3UTR P-PMO were tolerant of extensive mutations and deletions (10). Our results appear to confirm that result. The relative lack of activity of the three compounds targeted near the 3' terminus of the genome may indicate that the processing minus-strand polymerase complex displaces bound P-PMO or that P-PMO compete inefficiently with viral and host proteins for binding in this region (16, 21, 27, 35).

The most effective P-PMO targeted the transcription regulatory sequence. Two different P-PMO, TRS1 and TRS2, showed the highest levels of antiviral activity compared to all other P-PMO used in this study. The 20-mer TRS1 and 21-mer TRS2 vary by only a few nucleotides, as shown in Fig. 1, but are predicted to vary considerably in the targets to which they can bind. The TRS1 target includes the consensus TRS core sequence ACGAAC and 14 bases in the viral 5' direction. TRS2 covers the TRS core, four bases in the 3' direction, and 11 bases on the 5' side. This difference is predicted to allow binding of TRS1 to full-length genomic RNA and all eight of the subgenomic mRNAs (27). Out of the eight SARS subgenomic RNAs, five have start codons either adjacent to or within two bases of the TRS core (27). The 3' end of the TRS core is also the 3' end of the TRS1 target. TRS1 was therefore expected to have a more profound antiviral effect due to its potential for translational inhibition via duplexing to a region immediately upstream of the AUG translation start sites of at least five discrete viral RNAs combined with its potential ability to block discontinuous transcription of all subgenomic minus-strand RNAs. The TRS2 P-PMO spans the flanking sequence on both sides of the TRS core more extensively than TRS1 P-PMO and may therefore be more effective at inhibiting discontinuous transcription. The observation that TRS2 is more efficacious than TRS1 suggests that targeting the genomic RNA exclusively is a more efficient antiviral strategy with this class of antisense compound.

The SARS-CoV was able to partially escape inhibition by the TRS2 P-PMO within four viral passages. The forced generation of resistance suggests antisense agents as a powerful means of investigating virus structure and function and as a complement to traditional reverse-genetic studies. Furthermore, the observation that the TRS2-resistant SARS-CoV showed a reduced level of cytopathology opens the possibility for a new approach to the generation of attenuated viral strains. The results presented here indicate that the selection of therapeutic antisense antiviral targets will present the greatest opportunity for success when informed by detailed molecular understanding of the physical and temporal requirements for virus amplification.

#### ACKNOWLEDGMENTS

We thank the Chemistry Dept. at AVI BioPharma Inc. for expert synthesis, purification, and analysis of P-PMO and Jennifer Abma and Joey Ting for technical assistance with viral assays.

These studies were supported by NIH grants AI25913 (M.J.B.), AI43103 (M.J.B.), and NS41219 (B.W.N. and M.J.C.) and by NIH-NIAID contract HHSN 266200400058C "Functional and Structural Proteomics of the SARS-CoV."

#### REFERENCES

1. Bacha, U., J. Barrila, A. Velazquez-Campoy, S. A. Leavitt, and E. Freire. 2004. Identification of novel inhibitors of the SARS coronavirus main protease 3CLpro. *Biochemistry* **43**:4906–4912.
2. Benedetto, A., G. B. Rossi, C. Amici, F. Belardelli, L. Cioe, G. Carruba, and L. Carrasco. 1980. Inhibition of animal virus production by means of translation inhibitors unable to penetrate normal cells. *Virology* **106**:123–132.
3. Bosch, B. J., B. E. Martina, R. Van Der Zee, J. Lepault, B. J. Haijema, C. Versluis, A. J. Heck, R. De Groot, A. D. Osterhaus, and P. J. Rottier. 2004. Severe acute respiratory syndrome coronavirus (SARS-CoV) infection inhibition using spike protein heptad repeat-derived peptides. *Proc. Natl. Acad. Sci. USA* **101**:8455–8460.
4. Buchmeier, M. J., J. H. Elder, and M. B. Oldstone. 1978. Protein structure of lymphocytic choriomeningitis virus: identification of the virus structural and cell associated polypeptides. *Virology* **89**:133–145.
5. Chang, R. Y., M. A. Hofmann, P. B. Sethna, and D. A. Brian. 1994. A cis-acting function for the coronavirus leader in defective interfering RNA replication. *J. Virol.* **68**:8223–8231.
6. Dalton, K., R. Casais, K. Shaw, K. Stirrups, S. Evans, P. Britton, T. D. Brown, and D. Cavanagh. 2001. cis-acting sequences required for coronavirus infectious bronchitis virus defective-RNA replication and packaging. *J. Virol.* **75**:125–133.
7. Denison, M. R., B. Yount, S. M. Brockway, R. L. Graham, A. C. Sims, X. Lu, and R. S. Baric. 2004. Cleavage between replicase proteins p28 and p65 of mouse hepatitis virus is not required for virus replication. *J. Virol.* **78**:5957–5965.
8. Gallagher, T. M., M. J. Buchmeier, and S. Perlman. 1992. Cell receptor-independent infection by a neurotropic murine coronavirus. *Virology* **191**:517–522.
9. Giles, R. V., D. G. Spiller, R. E. Clark, and D. M. Tidd. 1999. Antisense morpholino oligonucleotide analog induces missplicing of C-myc mRNA. *Antisense Nucleic Acid Drug Dev.* **9**:213–220.
10. Goebel, S. J., B. Hsue, T. F. Dombrowski, and P. S. Masters. 2004. Characterization of the RNA components of a putative molecular switch in the 3' untranslated region of the murine coronavirus genome. *J. Virol.* **78**:669–682.
11. Hsue, B., T. Hartshorne, and P. S. Masters. 2000. Characterization of an essential RNA secondary structure in the 3' untranslated region of the murine coronavirus genome. *J. Virol.* **74**:6911–6921.
12. Hsue, B., and P. S. Masters. 1997. A bulged stem-loop structure in the 3' untranslated region of the genome of the coronavirus mouse hepatitis virus is essential for replication. *J. Virol.* **71**:7567–7578.
13. Hsue, B., and P. S. Masters. 1998. An essential secondary structure in the 3' untranslated region of the mouse hepatitis virus genome. *Adv. Exp. Med. Biol.* **440**:297–302.
14. Ingallinella, P., E. Bianchi, M. Finotto, G. Cantoni, D. M. Eckert, V. M. Supekar, C. Bruckmann, A. Carfi, and A. Pessi. 2004. Structural characterization of the fusion-active complex of severe acute respiratory syndrome (SARS) coronavirus. *Proc. Natl. Acad. Sci. USA* **101**:8709–8714.
15. Izeta, A., C. Smerdou, S. Alonso, Z. Penzes, A. Mendez, J. Plana-Duran, and L. Enjuanes. 1999. Replication and packaging of transmissible gastroenteritis coronavirus-derived synthetic minigenomes. *J. Virol.* **73**:1535–1545.
16. Johnson, R. F., and J. L. Leibowitz. 2001. Mutagenesis of the 3'42 nucleotide host protein binding element of the MHV 3'UTR. *Adv. Exp. Med. Biol.* **494**:499–505.
17. Jonassen, C. M., T. O. Jonassen, and B. Grinde. 1998. A common RNA motif in the 3' end of the genomes of astroviruses, avian infectious bronchitis virus and an equine rhinovirus. *J. Gen. Virol.* **79**:715–718.
18. Kamikubo, Y., R. De Guzman, G. Kroon, S. Curriden, J. G. Neels, M. J. Churchill, P. Dawson, S. Oldziej, A. Jagielska, H. A. Scheraga, D. J. Loskut-off, and H. J. Dyson. 2004. Disulfide bonding arrangements in active forms of the somatomedin B domain of human vitronectin. *Biochemistry* **43**:6519–6534.
19. Kao, R. Y., A. P. To, L. W. Ng, W. H. Tsui, T. S. Lee, H. W. Tsoi, and K. Y. Yuen. 2004. Characterization of SARS-CoV main protease and identification of biologically active small molecule inhibitors using a continuous fluorescence-based assay. *FEBS Lett.* **576**:325–330.
20. Kao, R. Y., W. H. Tsui, T. S. Lee, J. A. Tanner, R. M. Watt, J. D. Huang, L. Hu, G. Chen, Z. Chen, L. Zhang, T. He, K. H. Chan, H. Tse, A. P. To, L. W. Ng, B. C. Wong, H. W. Tsoi, D. Yang, D. D. Ho, and K. Y. Yuen. 2004. Identification of novel small-molecule inhibitors of severe acute respiratory syndrome-associated coronavirus by chemical genetics. *Chem. Biol.* **11**:1293–1299.
21. Liu, Q., R. F. Johnson, and J. L. Leibowitz. 2001. Secondary structural elements within the 3' untranslated region of mouse hepatitis virus strain JHM genomic RNA. *J. Virol.* **75**:12105–12113.
22. Liu, S., G. Xiao, Y. Chen, Y. He, J. Niu, C. R. Escalante, H. Xiong, J. Farmar, A. K. Debnath, P. Tien, and S. Jiang. 2004. Interaction between heptad repeat 1 and 2 regions in spike protein of SARS-associated coronavirus: implications for virus fusogenic mechanism and identification of fusion inhibitors. *Lancet* **363**:938–947.
23. Lu, X., Q. Yu, G. K. Binder, Z. Chen, T. Slepishkina, J. Rossi, and B.



- Dropulic.** 2004. Antisense-mediated inhibition of human immunodeficiency virus (HIV) replication by use of an HIV type 1-based vector results in severely attenuated mutants incapable of developing resistance. *J. Virol.* **78**:7079–7088.
24. Marra, M. A., S. J. Jones, C. R. Astell, R. A. Holt, A. Brooks-Wilson, Y. S. Butterfield, J. Khattri, J. K. Asano, S. A. Barber, S. Y. Chan, A. Cloutier, S. M. Coughlin, D. Freeman, N. Girn, O. L. Griffith, S. R. Leach, M. Mayo, H. McDonald, S. B. Montgomery, P. K. Pandoh, A. S. Petrescu, A. G. Robertson, J. E. Schein, A. Siddiqui, D. E. Smailus, J. M. Stott, G. S. Yang, F. Plummer, A. Andonov, H. Artsob, N. Bastien, K. Bernard, T. F. Booth, D. Bowness, M. Czub, M. Drebot, L. Fernando, R. Flick, M. Garbutt, M. Gray, A. Grolla, S. Jones, H. Feldmann, A. Meyers, A. Kabani, Y. Li, S. Normand, U. Stroher, G. A. Tipples, S. Tyler, R. Vogrig, D. Ward, B. Watson, R. C. Brunham, M. Krajden, M. Petric, D. M. Skowronski, C. Upton, and R. L. Roper. 2003. The Genome sequence of the SARS-associated coronavirus. *Science* **300**:1399–1404.
  25. Moulton, H. M., M. C. Hase, K. M. Smith, and P. L. Iversen. 2003. HIV Tat peptide enhances cellular delivery of antisense morpholino oligomers. *Antisense Nucleic Acid Drug Dev.* **13**:31–43.
  26. Moulton, H. M., M. H. Nelson, S. A. Hatlevig, M. T. Reddy, and P. L. Iversen. 2004. Cellular uptake of antisense morpholino oligomers conjugated to arginine-rich peptides. *Bioconjug. Chem.* **15**:290–299.
  27. Nanda, S. K., and J. L. Leibowitz. 2001. Mitochondrial aconitase binds to the 3' untranslated region of the mouse hepatitis virus genome. *J. Virol.* **75**:3352–3362.
  28. Nasevicius, A., and S. C. Ekker. 2000. Effective targeted gene 'knockdown' in zebrafish. *Nat. Genet.* **26**:216–220.
  29. Neuman, B. W., D. A. Stein, A. D. Kroeker, A. D. Paulino, H. M. Moulton, P. L. Iversen, and M. J. Buchmeier. 2004. Antisense morpholino-oligomers directed against the 5' end of the genome inhibit coronavirus proliferation and growth. *J. Virol.* **78**:5891–5899.
  30. Pasternak, A. O., E. van den Born, W. J. Spaan, and E. J. Snijder. 2003. The stability of the duplex between sense and antisense transcription-regulating sequences is a crucial factor in arterivirus subgenomic mRNA synthesis. *J. Virol.* **77**:1175–1183.
  31. Sawicki, S. G., and D. L. Sawicki. 1990. Coronavirus transcription: subgenomic mouse hepatitis virus replicative intermediates function in RNA synthesis. *J. Virol.* **64**:1050–1056.
  32. Sawicki, S. G., and D. L. Sawicki. 1995. Coronaviruses use discontinuous extension for synthesis of subgenome-length negative strands. *Adv. Exp. Med. Biol.* **380**:499–506.
  33. Siddell, S. G. 1995. The *Coronaviridae*: an introduction, p. 1–9. In S. G. Siddell (ed.), *The Coronaviridae*. Plenum Press, New York, NY.
  34. Snijder, E. J., P. J. Bredenbeek, J. C. Dobbe, V. Thiel, J. Ziebuhr, L. L. Poon, Y. Guan, M. Rozanov, W. J. Spaan, and A. E. Gorbalenya. 2003. Unique and conserved features of genome and proteome of SARS-coronavirus, an early split-off from the coronavirus group 2 lineage. *J. Mol. Biol.* **331**:991–1004.
  35. Spagnolo, J. F., and B. G. Hogue. 2000. Host protein interactions with the 3' end of bovine coronavirus RNA and the requirement of the poly(A) tail for coronavirus defective genome replication. *J. Virol.* **74**:5053–5065.
  36. Stein, D., E. Foster, S. B. Huang, D. Weller, and J. Summerton. 1997. A specificity comparison of four antisense types: morpholino, 2'-O-methyl RNA, DNA, and phosphorothioate DNA. *Antisense Nucleic Acid Drug Dev.* **7**:151–157.
  37. Summerton, J. 1999. Morpholino antisense oligomers: the case for an RNase H-independent structural type. *Biochim. Biophys. Acta* **1489**:141–158.
  38. Summerton, J., and D. Weller. 1997. Morpholino antisense oligomers: design, preparation, and properties. *Antisense Nucleic Acid Drug Dev.* **7**:187–195.
  39. Thiel, V., K. A. Ivanov, A. Putics, T. Hertzog, B. Schelle, S. Bayer, B. Weissbrich, E. J. Snijder, H. Rabenau, H. W. Doerr, A. E. Gorbalenya, and J. Ziebuhr. 2003. Mechanisms and enzymes involved in SARS coronavirus genome expression. *J. Gen. Virol.* **84**:2305–2315.
  40. Van Den Born, E., A. P. Gultyaev, and E. J. Snijder. 2004. Secondary structure and function of the 5'-proximal region of the equine arteritis virus RNA genome. *RNA* **10**:424–437.
  41. van Heeswijk, R. P., A. Veldkamp, J. W. Mulder, P. L. Meenhorst, J. M. Lange, J. H. Beijnen, and R. M. Hoetelmans. 2001. Combination of protease inhibitors for the treatment of HIV-1-infected patients: a review of pharmacokinetics and clinical experience. *Antivir. Ther.* **6**:201–229.
  42. Wang, Z., L. Ren, X. Zhao, T. Hung, A. Meng, J. Wang, and Y. G. Chen. 2004. Inhibition of severe acute respiratory syndrome virus replication by small interfering RNAs in mammalian cells. *J. Virol.* **78**:7523–7527.
  43. Westerhout, E. M., M. Ooms, M. Vink, A. T. Das, and B. Berkhout. 2005. HIV-1 can escape from RNA interference by evolving an alternative structure in its RNA genome. *Nucleic Acids Res.* **33**:796–804.
  44. Wu, C. Y., J. T. Jan, S. H. Ma, C. J. Kuo, H. F. Juan, Y. S. Cheng, H. H. Hsu, H. C. Huang, D. Wu, A. Brik, F. S. Liang, R. S. Liu, J. M. Fang, S. T. Chen, P. H. Liang, and C. H. Wong. 2004. Small molecules targeting severe acute respiratory syndrome human coronavirus. *Proc. Natl. Acad. Sci. USA* **101**:10012–10017.
  45. Yi, L., Z. Li, K. Yuan, X. Qu, J. Chen, G. Wang, H. Zhang, H. Luo, L. Zhu, P. Jiang, L. Chen, Y. Shen, M. Luo, G. Zuo, J. Hu, D. Duan, Y. Nie, X. Shi, W. Wang, Y. Han, T. Li, Y. Liu, M. Ding, H. Deng, and X. Xu. 2004. Small molecules blocking the entry of severe acute respiratory syndrome coronavirus into host cells. *J. Virol.* **78**:11334–11339.
  46. Yokomori, K., M. Asanaka, S. A. Stohman, S. Makino, R. A. Shubin, W. Gilmore, L. P. Weiner, F. I. Wang, and M. M. Lai. 1995. Neuropathogenicity of mouse hepatitis virus JHM isolates differing in hemagglutinin-esterase protein expression. *J. Neurovirol.* **1**:330–339.
  47. Yuan, K., L. Yi, J. Chen, X. Qu, T. Qing, X. Rao, P. Jiang, J. Hu, Z. Xiong, Y. Nie, X. Shi, W. Wang, C. Ling, X. Yin, K. Fan, L. Lai, M. Ding, and H. Deng. 2004. Suppression of SARS-CoV entry by peptides corresponding to heptad regions on spike glycoprotein. *Biochem. Biophys. Res. Commun.* **319**:746–752.
  48. Zhang, Y., T. Li, L. Fu, C. Yu, Y. Li, X. Xu, Y. Wang, H. Ning, S. Zhang, W. Chen, L. A. Babiuk, and Z. Chang. 2004. Silencing SARS-CoV Spike protein expression in cultured cells by RNA interference. *FEBS Lett.* **560**:141–146.
  49. Zuker, M. 2003. Mfold web server for nucleic acid folding and hybridization prediction. *Nucleic Acids Res.* **31**:3406–3415.